

Virtual impedance-based frequency decoupling for modular fuel cell-battery DC shipboard power systems

Kopka, Timon; Coraddu, Andrea; Polinder, Henk

DOI

[10.1080/20464177.2025.2489313](https://doi.org/10.1080/20464177.2025.2489313)

Publication date

2025

Document Version

Final published version

Published in

Journal of Marine Engineering and Technology

Citation (APA)

Kopka, T., Coraddu, A., & Polinder, H. (2025). Virtual impedance-based frequency decoupling for modular fuel cell-battery DC shipboard power systems. *Journal of Marine Engineering and Technology*. <https://doi.org/10.1080/20464177.2025.2489313>

Important note

To cite this publication, please use the final published version (if applicable). Please check the document version above.

Copyright

Other than for strictly personal use, it is not permitted to download, forward or distribute the text or part of it, without the consent of the author(s) and/or copyright holder(s), unless the work is under an open content license such as Creative Commons.

Takedown policy

Please contact us and provide details if you believe this document breaches copyrights. We will remove access to the work immediately and investigate your claim.



Virtual impedance-based frequency decoupling for modular fuel cell-battery DC shipboard power systems

Timon Kopka, Andrea Coraddu & Henk Polinder

To cite this article: Timon Kopka, Andrea Coraddu & Henk Polinder (09 Apr 2025): Virtual impedance-based frequency decoupling for modular fuel cell-battery DC shipboard power systems, Journal of Marine Engineering & Technology, DOI: [10.1080/20464177.2025.2489313](https://doi.org/10.1080/20464177.2025.2489313)

To link to this article: <https://doi.org/10.1080/20464177.2025.2489313>



© 2025 The Author(s). Published by Informa UK Limited, trading as Taylor & Francis Group.



Published online: 09 Apr 2025.



Submit your article to this journal [↗](#)



Article views: 85



View related articles [↗](#)



View Crossmark data [↗](#)

Virtual impedance-based frequency decoupling for modular fuel cell-battery DC shipboard power systems

Timon Kopka ^a, Andrea Coraddu^{a,b} and Henk Polinder^a

^aDepartment of Maritime and Transport Technology, Delft University of Technology, Delft, The Netherlands; ^bNetherlands Defence Academy, Den Helder, The Netherlands

ABSTRACT

In the scope of the energy transition, the maritime industry, still heavily relying on fossil fuels, is facing expectations to reduce its carbon output. Electrified shipboard power systems (SPSs) equipped with hydrogen fuel cells (FCs) and energy storage systems (ESSs) are a promising solution for the shift to zero-emission shipping. A remaining challenge is the efficient coordination of multiple parallel power generation and storage modules. This article proposes a modular approach to the power system control to offer a plug-and-play capability for multiple FCs and ESSs, facilitating a topology reconfiguration. Virtual impedance-based droop is implemented to achieve power sharing and load frequency decoupling in a decentralised architecture. An additional low-bandwidth communication is leveraged to enable parameter adaptation after a topology reconfiguration. The methodology is tested numerically with a short-sea cargo vessel serving as a case study. The local controllers are tuned to achieve load frequency decoupling between FCs and batteries matching the specified time constant. For a maneuvering power profile, the average FC power gradient could be decreased by 36%, limiting their degradation caused by dynamic operation, while increasing the depth-of-discharge of the batteries. The simulations further show that an adaptation of control parameters after a component fault can be used to maintain the system's voltage dynamics. The voltage drop caused by a load step in a reconfigured system that disconnected one of two ESS could be reduced by 37.5% by control parameter adaptation.

ARTICLE HISTORY

Received 28 March 2024
Accepted 28 March 2025

KEYWORDS

DC power distribution;
frequency decoupling; fuel
cells; power sharing;
shipboard power systems

1. Introduction

The design of modern shipboard power systems (SPSs) is driven by multiple factors, including technological advances, new regulations, as well as economic and environmental aspects (Hansen and Wendt 2015). A key development is the electrification of ships, away from conventional diesel-mechanic propulsion and towards a utilisation of novel energy sources and energy storage systems (ESSs) (Mutarraf et al. 2018). The goal to decrease carbon emissions has increased interest in alternative energy carriers and converters, among which hydrogen fuel cells (FCs) are a promising option (Nuchturee et al. 2020; van Biert et al. 2016).

In this context, DC distribution with power electronics interfaces is a fitting solution for the integration of multiple different energy supply and storage technologies (Latorre et al. 2023). This yields high controllability of power flows in the system (Xu et al. 2022). The efficient coordination of all devices, based on their respective characteristics is key (Xu et al. 2022). The system control must facilitate the balance between the fluctuating load and generation while keeping fuel consumption and degradation on the components at a minimum (Han et al. 2019). Especially the FCs' lifetime is affected by their operation, which ideally is at low current gradients within its efficient output range (Shakeri et al. 2020).

DC distribution and power converters facilitate an easy expansion and reconfiguration of the power system topology, promoting a modular design with plug-and-play characteristics (Sadabadi et al. 2018; Xing et al. 2021). This also requires the control system to be modular,

and adapt to a reconfiguration, e.g. during regular operation, after a fault, or system retrofit.

To implement a scalable and reconfigurable control strategy, a decentralised architecture can be used (Dragicevic et al. 2015; Xiao et al. 2022). Doing so removes the need for an extensive communication architecture, enables the local implementation of main control functionalities, and reduces vulnerability to faults. The conventional decentralised method is virtual impedance-based droop control (Zahedi and Norum 2013b sep; Han et al. 2019), in DC systems implemented as voltage droop. Major drawbacks of droop control are a steady-state deviation from the set-point and imbalances in power-sharing. Further, standard voltage droop does not consider the time response of different sources, which is an important aspect in the control design with ESS (Xu et al. 2017). It is desirable to decouple the main power source from the load using the ESS, so the main supply can operate at low power gradients and in an efficient operating point (Mutarraf et al. 2018).

The literature on coordinated control and system stabilisation for FC-battery SPS is dominated by centralised approaches, focussing the power split between a single FC system and ESS. This is realised, e.g. using PI-controllers as in Su et al. (2014), Chen et al. (2020) and Balestra and Schjølberg (2021) or via rule-based approaches as in Han et al. (2014), Balestra and Schjølberg (2021), Bassam et al. (2017) and Zhu et al. (2014 mar).

The above-mentioned load-frequency separation is also an important objective for the power split in hybrid ESS including both batteries and ultra-capacitors, as proposed by Jin et al. (2017 mar),

Kwon et al. (2020 jun) and Xie et al. (2022) which can be adapted for the control in FC-battery designs.

The proposed solutions, however, do not cover investigations of larger power systems with multiple FCs and batteries, or even a modular topology. A centralised controller computing all power references is not applicable here due to the overhead required for fast communication. For this reason, this study proposes a decentralised method for dynamic power sharing among multiple power sources with different time characteristics. The proposed scheme can adapt to the system reconfiguration in a plug-and-play manner.

This article expands on the previous work by Kopka et al. (2023), whose contributions are summarised as follows.

- (1) A virtual impedance-based approach with both capacitive and inductive elements to achieve a decentralised voltage stabilisation with frequency decoupling in a FC-battery DC SPS.
- (2) An extension of local controllers by voltage restoration and state of charge (SoC) management functionalities via adaptation of the reference voltage.
- (3) Demonstration of the control strategy using real measurements at the example of a virtually retrofitted short-sea cargo vessel

In addition, this article delves into the concept of modularity and proposes an extension of the previously developed strategy by a low-bandwidth communication network to adapt the control parameters following a topology reconfiguration. For this purpose, how the local control parameters can be adapted after a component fault is investigated in order to maintain the desired power system dynamics. Furthermore, this work presents additional simulation results using high-frequency measurements from multiple operating scenarios.

This paper is organised as follows. A virtual retrofit and the modelling of a reference vessel with a FC-battery hybrid system is introduced in Section 2. Subsequently, the proposed decentralised control strategy for coordinating FCs and batteries is laid out in Section 3. Section 4 describes the simulation environment for numerical investigations and discusses the obtained results. The main conclusions are presented in Section 5.

2. System description

The work in this article focuses on all-electric ships with a hybrid energy system, as defined in Geertsma et al. (2017), consisting of multiple main power supplies and ESSs. The emphasis is on FC-battery hybrid SPS, however, the method is applicable to alternative generation and storage technologies as well. This section describes the case study used in this work and introduces the models used for numerical investigations of the SPS.

2.1. Reference vessel

The originally diesel-driven short-sea cargo vessel *Ankie* operating in the Baltic and North Seas serves as the reference vessel for the case study. The main specifications of the vessel are listed in Table 1. The original power system utilises a main diesel engine, mechanically connected to a controllable pitch propeller. Additionally, a shaft generator is used as a power take-off to feed the bow thruster, auxiliary, and hotel loads via an electric AC distribution network. The system is equipped with an auxiliary engine that can be used for supplying the electric system while the main engine is turned off.

The reference vessel is equipped with measurement devices, continually logging the power generation of main and auxiliary engines, main consumers, as well as mechanical power working on the propulsion shaft. Figures 1 and 2 show the histograms of total power consumption and speed over ground for one month of continuous

Table 1. Specifications of reference vessel.

Parameter	Info
Type	General cargo ship
Length	90.0 m
Width	12.6 m
DWT	3638 t
Propulsion	Diesel-mechanic
Main Engine	Wärtsilä 9L20 (1.6 MW)

Note: Adapted from Mylonopoulos et al. (2024).

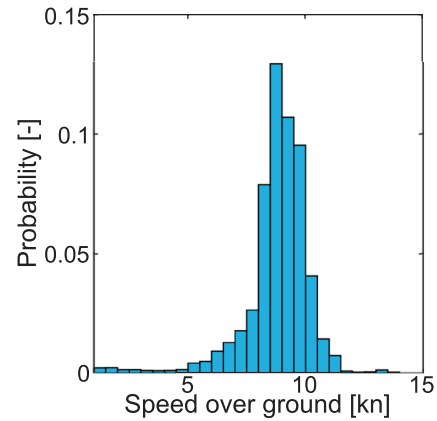


Figure 1. Histogram of speed over ground of reference vessel derived from continuous measurements over one month.

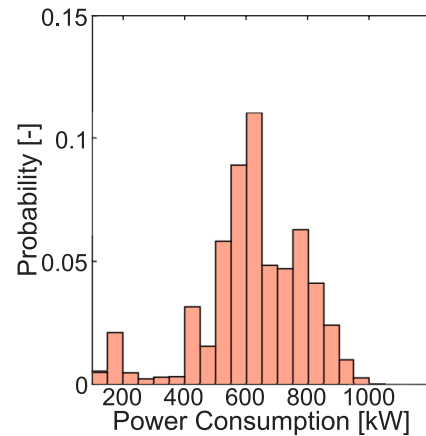


Figure 2. Histogram of power consumption of reference vessel derived from continuous measurements over one month.

logging. Time spent at low power (<100 kW; 41.7% of samples) and at low speed (<1 kn; 44.0% of samples) are not shown in the figures. The measurements are available with a sampling time of 200 ms, which is considerably faster than typical ramp times of power generators and conventional propulsion systems in ships. Power profiles for different operation scenarios can be derived from the measurements and used as input for the re-design and simulation of a retrofitted vessel.

2.2. Virtual retrofit

Since the SPS of the original vessel does not match the scope of this work, a virtual retrofit of the power system was conducted to make it usable as a case study. In the virtual retrofit the vessel is fitted with an FC-battery hybrid system. Hence, all diesel-generators are

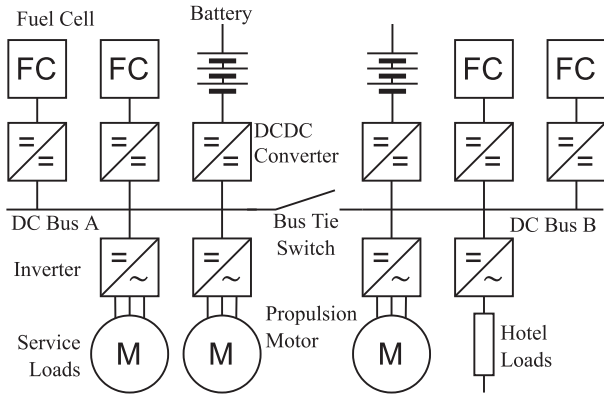


Figure 3. Topology of retrofitted hydrogen-based system with electric propulsion and DC distribution.

Table 2. Parameters of retrofitted power system components.

Parameter	Description	Value
$P_{r,fc}$	FC power rating	4x325 kW
E_{bat}	Battery energy capacity	2x225 kWh
$C_{bat,chg}$	Battery max. charge C-rate	1.5
$C_{bat,dis}$	Battery max. discharge C-rate	1.5
$P_{r,bat}$	Battery power rating	2x337.5 kW
P_{em}	Prop. motor rating	2x600 kW

removed from the system, and an electric-driven propeller replaces the mechanic propulsion. The resulting system, equipped with four FC and two battery systems in a dual-bus configuration, is shown in Figure 3. This constellation creates a redundancy to compensate for a component or bus fault, and the number of FCs in the system gives operational flexibility. All power generation devices and loads are connected to the electric system, forming an integrated power system. DC distribution is used for the on-board grid, as it matches the outputs of FCs and batteries, among further advantages, such as increased efficiency (Zahedi et al. 2014) and operational flexibility (Xu et al. 2022). Neglecting the enhanced operational capabilities of electric propulsion drives, it is assumed that the load requirements of the vessel remain the same as in the original topology.

The power and energy ratings of the components are listed in Table 2. The FC and battery ratings are based on a newly developed short-sea cargo vessel fuelled by liquid hydrogen that has similar operational characteristics as the *Ankie*. The power rating of the batteries is sufficient such that the ESS can compensate for the fault of FC system while having surplus capacity for covering transient loads. Furthermore, the energy rating allows short-time strategic charging and load levelling to reduce the power gradients of the FCs.

2.3. Modelling

The focus of this work is the development of control strategies. Power system and component models are required to evaluate these strategies. Because the emphasis is on system-level control, simple dynamic models are implemented to build a simulation environment for the complete SPS. The following sections describe the approaches for modelling FCs, batteries, converters, and loads and how they interact with one another via the DC bus.

2.3.1. Proton exchange-membrane fuel cells

The FC models used in this work were implemented according to Njoya et al. (2009 sep). A beneficial feature of this model is that

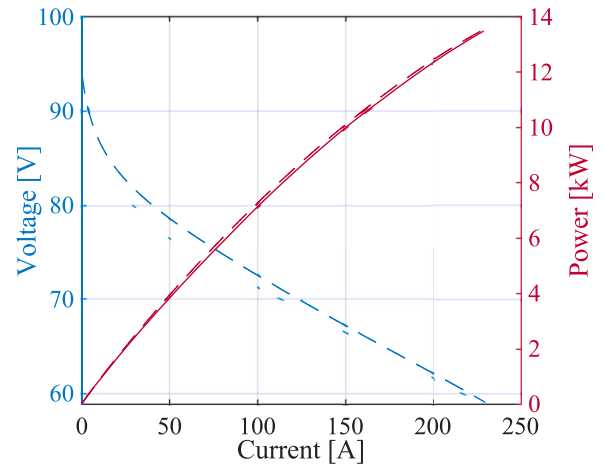


Figure 4. Polarization curve and power output of Nedstack FCS 13 XXL module, from data-sheet and simulation in steady-state.

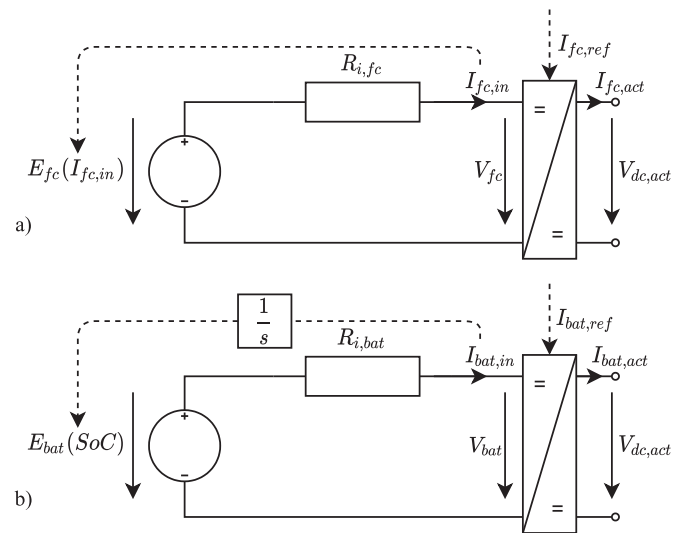


Figure 5. Equivalent circuit models of FC (a) and battery (b) including DC-DC converter and interface to the DC bus.

it can be parameterised using manufacturer data. Hence, the real components can be easily represented.

The FC systems investigated in this paper are based on the Nedstack FCS 13 XXL, a proton-exchange membrane fuel cell (PEMFC) module with a maximum output power of 13.6 kW (Nedstack 2023). Figure 4 shows the polarisation curves and power outputs of a single module from the manufacturer's data-sheet against the simulation results obtained using the described model in steady-state operation. The graph describes the relationship between the FC current $I_{fc,in}$ and voltage V_{fc} , as indicated in Figure 5(a). The mean absolute percentage error (MAPE) of the output voltage between the simulation and data-sheet is 1.6%, which is sufficiently accurate for the purpose of this research. To achieve the targeted 325 kW per FC system in the SPS, 24 modules are stacked together.

2.3.2. Li-Ion batteries

For the batteries, a model of similarly low fidelity as that for the FCs was used, as reported in Tremblay et al. (2007 sep), shown here in Figure 5(b). It is based on single cell modelling, and in this study, generic values for Li-ion battery cells, as reported in the source, are used. Opposed to the FC model, the voltage source E_{bat} is a function

of the SoC, which is obtained via Coulomb counting. Multiple cells are connected in series and parallel to achieve the desired voltage, power, and energy levels of the battery packs.

2.3.3. DC-DC converters

A dynamic model of a DC-DC converter for maritime power systems is presented in Zahedi and Norum (2013a). It is an averaged model that describes the current dynamics while neglecting any losses in the system. Similarly, an averaged representation of a half-bridge is used in Haseltalab et al. (2021).

Conventionally, the converter is current-controlled using PI feedback control, as outlined in Mokhtar et al. (2019). For DC SPSs, the current control bandwidth is typically in the range of 1000 Hz (Zeng et al. 2022). Whereas transient analysis requires a high-fidelity model of the power converters, the system-level simulation and investigation of voltage droop control allow the simplified representation of the current control using a first-order low-pass filter (Lu et al. 2014). The converter output current $I_{out,act}$ as a function of reference current $I_{out,ref}$ and current control time constant τ_{cc} is realised according to

$$I_{out,act} = \frac{1}{s\tau_{cc} + 1} I_{out,ref} \quad (1)$$

Consequently, the input-side current I_{in} as a function of $I_{out,act}$ as well as input and DC bus voltages V_{in} and $V_{dc,act}$, as indicated in Figure 5 is computed as

$$I_{in} = \frac{V_{dc,act}}{V_{in}} I_{out,act} \quad (2)$$

2.3.4. Loads

All system loads are aggregated and represented as a power load P_{load} acting on the electric system. The load profile obtained from the measurements represents the actual consumed power and is modelled as an exogenous input disturbance. Assuming that all loads are tightly power-controlled, the current drawn by the loads I_{load} depends on the actual bus voltage $V_{dc,act}$. Accordingly, the current drawn by the loads is derived as

$$I_{load} = \frac{P_{load}}{V_{dc,act}} \quad (3)$$

2.3.5. DC distribution

The DC distribution system in a ship is characterised by short power lines with low impedance. Following the approach described in Xu et al. (2022), the bus in DC SPS can be simplified as a lumped capacitor, neglecting the losses and inductances in the network. The DC-link capacity C_{dc} is the sum of the output capacitors of all N adjacent DC-DC converters $C_{out,i}$. Accordingly, the time derivative of the DC-link voltage $\dot{V}_{dc,act}$ can be computed as

$$\dot{V}_{dc,act} = \frac{1}{C_{dc}} \left(\sum_{i=1}^N I_{out,i} - I_{load} \right) \quad (4)$$

$$C_{dc} = \sum_{i=1}^N C_{out,i} \quad (5)$$

3. Power system control

The control of the power system covers multiple functionalities, of which this work focuses on the coordinated control for stabilising the DC bus voltage and managing the power flows between the different components.

On the generation side, each primary system, i.e. the FC systems and batteries, is interfaced to the bus via a DC-DC converter.

Whereas the FCs can only provide positive current, the battery converter needs to be bi-directional to enable both discharging and charging. The converters are current-controlled, tracking a given reference value, as described in Section 2.3. Additionally, the local controllers ensure the operation of each device within its technical limitations, e.g. voltage and current limits. The balance-of-plant and inner control loops of the FC battery systems are not explicitly considered here.

This section leads through the proposed implementation of local controllers for FCs and batteries. A more detailed elaboration can be found in Kopka et al. (2023). This work additionally introduces a method for parameter adaptation after a topology change.

3.1. Coordinated control

The coordinated control layer covers a multitude of functionalities. This work focuses on the voltage stabilisation and restoration, battery SoC management, and power sharing among parallel devices. Additionally, this work explores the adaptation of control parameters to a reconfiguration of the power system topology.

For the control of the regarded SPS, FCs and batteries are required to match the power demand in dynamic conditions, stabilising the DC bus voltage. The FCs benefit from operation within a specific power band and at low power gradients to limit their lifetime degradation and operate them at a high efficiency (Ahmadi Sarbast 2021). The batteries can provide high power gradients and thereby cover load fluctuations, but cycling at high power and high depth-of-discharge also degrades their lifetime.

In this section, first a centralised controller is described as a benchmark strategy. Subsequently, a decentralised control architecture is proposed, employing virtual impedances for frequency decoupling between FCs and batteries.

3.2. Centralised control

Ideally, the current references for the coordination of FCs and batteries can be generated in a centralised controller. All required information about the system's states is available to the central controller so that it can compute a target for each component in real-time while accounting for their different characteristics. As a benchmark strategy, a PI feedback controller with a filter-based frequency decoupling is considered, similar to Kwon et al. (2020 jun). The PI feedback loop with gains k_p and k_i is employed for the voltage control, determining a total required current for bus stabilisation and restoration $I_{tot,ref}$ as a function of the voltage set-point error $V_{dc,ref} - V_{dc,act}$:

$$I_{tot,ref} = (V_{dc,ref} - V_{dc,act}) \left(k_p + \frac{k_i}{s} \right) \quad (6)$$

Low-frequency elements of this reference current are forwarded as a reference current for the FCs $I_{fc,ref}$, while the remaining high-frequency parts of the reference $I_{bat,ref}$ are to be covered by the batteries. The control strategy is illustrated in Figure 6. For the frequency decoupling, the filter is tuned using the time constant τ_{fd} .

$$I_{fc,ref} = \frac{I_{tot,ref}}{s\tau_{fd} + 1} \quad (7)$$

$$I_{bat,ref} = I_{tot,ref} - I_{fc,ref} \quad (8)$$

3.3. Decentralised control

Several issues make the implementation of real-time control in a centralised unit challenging. The acquisition of measurements

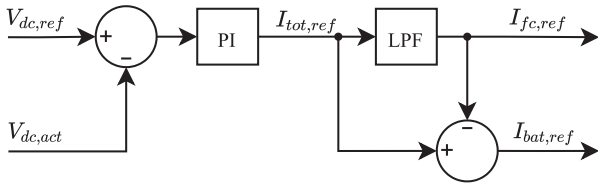


Figure 6. Centralised power sharing strategy with PI controller and low-pass filter.

and real-time distribution of reference signals to local controllers requires high-bandwidth communication, which can be costly, prone to faults, and introduce latencies. Hence, this work proposes the implementation of a decentralised architecture. No communication between local controllers is required for the real-time voltage stabilisation and restoration. This provides a control strategy which can be scaled to a modular reconfiguration of the power system topology. In the following, virtual impedance-based droop is introduced as a method for voltage stabilisation and frequency decoupling between the different sources. This method is subsequently extended by a voltage restoration and an SoC management functionality.

3.3.1. Virtual impedance-based droop

The state-of-the-art solution for decentralised voltage stabilisation in DC power systems is voltage droop (Gao et al. 2019). Whereas conventional, resistive droop control is appropriate for power sharing under steady-state conditions, additional capacitive or inductive droop elements can be used to include an additional time-response of the controllers (Chen et al. 2019; Khazaei 2021). Whereas a capacitive droop controller serves as a high-pass filter, this work proposes an extension of droop schemes with an inductive element to create a low-pass filter (LPF). Such a droop controller is an appropriate tool for controlling the power output of power supplies with slow dynamic capabilities, such as FCs. Figure 7 shows the equivalent circuits describing the functioning principle of different droop schemes. The corresponding transfer functions of the DC link voltage deviation $\Delta V = V_{d,ref} - V_{dc,act}$ to the current reference are as follows:

$$\frac{I_{d,rc}}{\Delta V} = \frac{sC_{d,rc}}{sR_{d,rc}C_{d,rc} + 1} \quad (9)$$

$$\frac{I_{d,rl}}{\Delta V} = \frac{1}{R_{d,rl} + sL_{d,rl}} \quad (10)$$

where $I_{d,x}$ is the computed reference current for the droop-controlled source. $R_{d,x}$, $C_{d,x}$, and $L_{d,x}$ describe the virtual resistance, capacitance and inductance, C_{dc} is the total dc bus capacity; $V_{d,ref}$ and $V_{dc,act}$ are the reference and actual dc bus voltages, respectively.

3.3.2. Voltage restoration

The aforementioned droop control schemes lead to a voltage drop on the main bus proportional to the delivered power (Peyghami et al. 2017). To restore the voltage and maintain the modular power system design, the voltage reference $V_{d,ref}$ in the local droop controllers is adapted based on an integral action on the set-point error and is computed as

$$V_{d,ref} = V_{dc,nom} + k_v \int V_{dc,nom} - V_{dc,act} dt \quad (11)$$

where k_v is the integral coefficient for voltage regulation.

3.3.3. SoC management

Due to the ESSs' limited energy capacity, the SoC of each device needs to be maintained within specified limits, e.g. between 20 % and

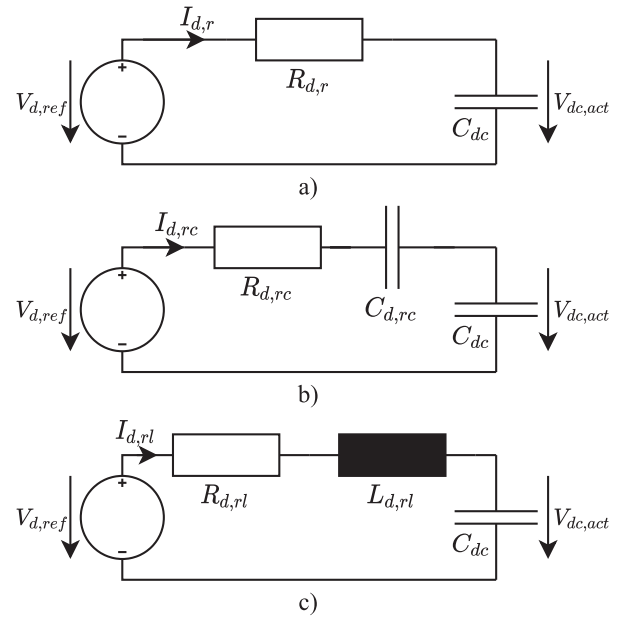


Figure 7. Equivalent circuit representations of decentralised droop controllers with (a) resistive (b) resistive-capacitive, and (c) resistive-inductive virtual impedance.

80 % as in Balestra (2022). Additionally, different SoCs in parallel devices need to be balanced. The local battery controllers are further extended to include the SoC management in the decentralised control strategy. Each local battery controller is enhanced by an SoC-dependent term $V_{SoC,ref}$, which manages the additional charge and discharge of the device. The reference voltage $V_{d,ref}^*$ is manipulated for this purpose and is computed as

$$V_{d,ref}^* = V_{d,ref} + V_{SoC,ref} \quad (12)$$

$$V_{SoC,ref} = k_{SoC} \int (SoC_{ref} - SoC_{act})^\alpha dt \quad (13)$$

where SoC_{ref} and SoC_{act} are the reference and actual SoC values and k_{SoC} is the integral coefficient of the SoC management strategy. An additional shape factor α describes the relationship between SoC deviation and charging current. Figure 8 shows the imposed discharge current for an ESS based on its SoC for different α . To ensure that the ESS current reaches its respective maximum and minimum values when the SoC reaches its limits k_{SoC} is computed as following. Here, it is assumed that the reference SoC is centred around maximum and minimum SoC and that the batteries maximum charge and discharge currents are equal at $I_{bat,max}$:

$$k_{SoC} = -\frac{I_{bat,max}}{C_{d,rc} \left(\frac{SoC_{max} - SoC_{min}}{2} \right)^\alpha} \quad (14)$$

3.3.4. Implementation

Figure 9 shows a graphical representation of the local controllers for the FCs and ESSs. Since no real-time communication takes place between the decentralised controllers, it is crucial to carefully tune all control parameters so that the overall system performance meets the desired requirements. To achieve the desired frequency separation, the resistive-inductive droop scheme from Equation (10) is used to control each individual FC system's output current, while each ESS is controlled according to the resistive-capacitive droop Equation (9).

For the consistent behaviour of the power system under dynamic operation, a series of guidelines for tuning the control parameters are

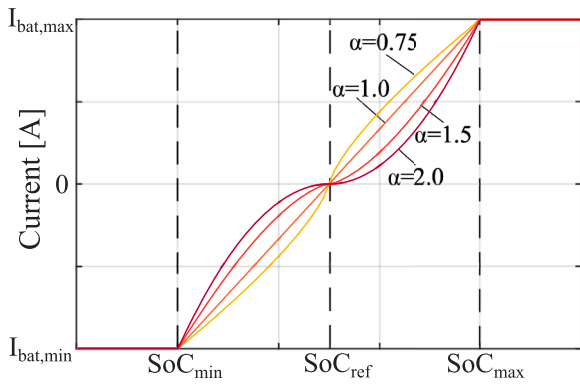


Figure 8. SoC-dependent charging current for each ESS for different shape factors α to track the reference value while avoiding over- and undercharging.

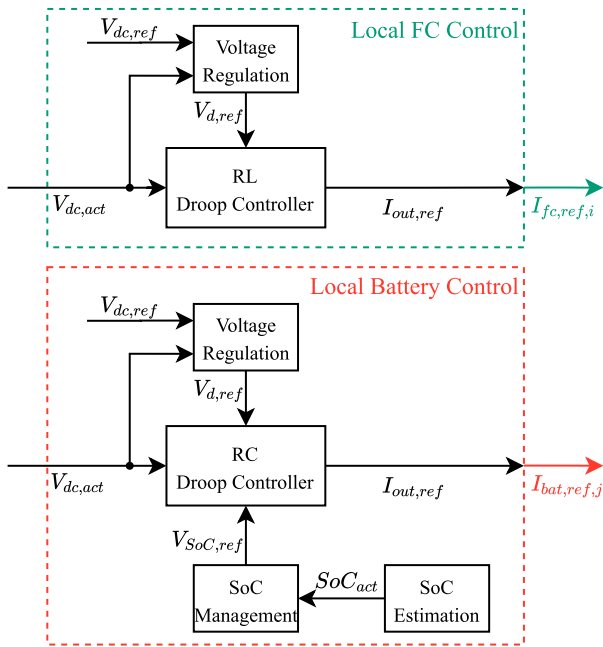


Figure 9. Synthesis of local controllers for FCs and batteries.

proposed. Following these guidelines ensures a coherent design of all local controllers:

- The total droop resistance of the main power supplies should equal the total droop resistance of the ESS and match a reference value $R_{d,ref}$ so that a consistent response of the power system in dynamic and steady-state operation is obtained.
- The total droop resistance should be selected such that the bandwidth of the DC bus voltage regulation is at least one order of magnitude slower than the current control of the DC-DC converters ($\tau_{vc} \gg \tau_{cc}$).
- The droop resistances of the FC controllers should be inversely proportional to their rated power. The same approach shall be applied for the ESS.
- In the proposed FC-hybrid system, the time constants of the RC and RL filters should be equal and match the desired frequency decoupling time constant τ_{fd} . This allows a smooth transition from batteries to FC as a power source.
- Reducing the time constant τ_{fd} will yield a higher dynamic capability, allowing the generation-side to cover higher load gradients, which would otherwise be inhibited by the limited power of

the batteries. However, a higher time constant lowers the output gradients of the FCs, reducing their degradation.

3.4. Low-bandwidth communication and reconfiguration

The proposed control strategy from Kopka et al. (2023) has a series of challenges due to the lack of information-sharing. The system's dynamics will differ from the designed characteristics once the topology changes, e.g. due to a component fault or an extension of the power system. It is furthermore inflexible towards a change in the topology. To mitigate this, this study proposes the extension of the decentralised strategy by a central controller and low-bandwidth communication and leveraging shared information for an adaptation of control parameters. It is important to note that the central controller is used only for slow information sharing, whereas all essential computations for coordinated control remain in the local controllers.

The response of each local controller is determined based on its virtual resistance and the time constant of the low- or high-pass filter constituted by the virtual impedance. The goal is for each local controller to adapt its parameters so that the total droop gain of the system matches its target value $R_{d,ref}$ independent of the system topology. Hence, the guidelines listed in Section 3.3.4 should hold true even if the topology is reconfigured.

Each FC system and battery shares its available power rating, $P_{r,fc,i}$ and $P_{r,bat,j}$ respectively, via the communication network. Accordingly, the central controller can determine the total available FC power $P_{r,fc,tot}$ and total available battery power $P_{r,bat,tot}$ as

$$P_{r,fc,tot} = \sum_{i \in N} P_{r,fc,i} \quad (15)$$

$$P_{r,bat,tot} = \sum_{j \in M} P_{r,bat,j} \quad (16)$$

In case a component fails, is degraded, or the system is reconfigured, the effect of the altered topology is visible in a change of the total available power ratings. The central controller broadcasts $P_{r,fc,tot}$, $P_{r,bat,tot}$, and reference values for τ_{fd} and k_v , as well as $R_{d,ref}$. Since a low-bandwidth communication is assumed here, and to avoid jumps in the parameters, the local controllers apply a low-pass filter with time constant 10 s on the received values. Each local controller is then able to compute its local virtual impedance parameters $R_{d,rl}$ and $C_{d,rl}$, or $R_{d,rc}$ and $C_{d,rc}$. The i th FC computes its control parameters as

$$R_{d,rl} = R_{d,ref} \frac{P_{r,bat,tot}}{P_{r,bat,j}} \quad (17)$$

$$L_{d,rl} = \tau_{fd} R_{d,rl} \quad (18)$$

The j th battery computes its control parameters as

$$R_{d,rc} = R_{d,ref} \frac{P_{r,bat,tot}}{P_{r,bat,j}} \quad (19)$$

$$C_{d,rc} = \frac{\tau_{fd}}{R_{d,rc}} \quad (20)$$

Additionally, it needs to be considered that the DC bus capacitance changes upon disconnection of a source, assuming that the switch is situated between the converters' output filter and the DC bus. As the total virtual droop $R_{d,ref}$ is dimensioned to reach a specific control time constant for the voltage stabilisation τ_{vc} , the total droop should be adjusted to achieve a consistent voltage control speed. Assuming that the central controller has an estimate of the total capacity in the

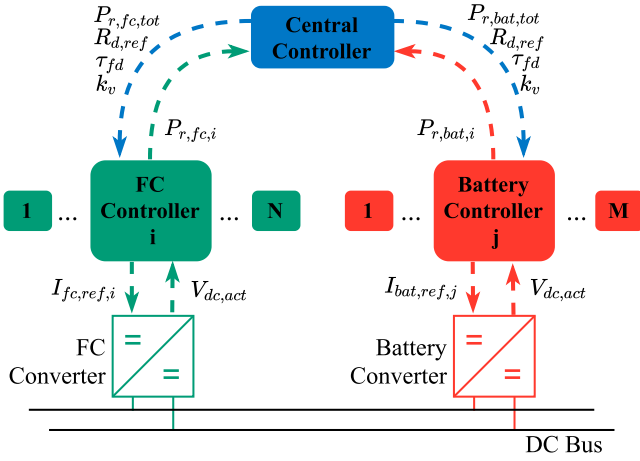


Figure 10. Control architecture of local FC and battery controllers and central controller communicating via low-bandwidth interface.

Table 3. System and control parameterisation for numerical investigations.

Parameter	Description	Value
$V_{dc,nom}$	Nominal DC bus voltage	700 V
$C_{out,fc}$	FC converter output capacity	25 mF
$C_{out,bat}$	Battery converter output capacity	25 mF
τ_{cc}	Current control time constant	1 ms
τ_{vc}	Voltage control time constant	10 ms
α	SoC shape factor	2.0 –
τ_{fd}	Frequency decoupling time constant	variable

bus $C_{dc,est}$, the total droop is adapted as

$$R_{d,ref} = \tau_{vc} C_{dc,est} \quad (21)$$

The information exchange between the central and local controllers in the power system is visualised in Figure 10. Since no vital computation is being done in the central controller and all adaptations based on information broadcast is low-bandwidth, a failure of the communication network has no immediate effect on the voltage stability of the system.

4. Numerical investigations

A power system model as outlined in Section 2.3 is implemented in Matlab/Simulink to create a simulation environment where control strategies can be tested. This section describes the case study and system parameterisation in more detail, introduces test scenarios for the control of the reference vessel and evaluates the numerical results obtained through the simulations. Table 3 provides an overview of system level parameters used throughout the simulations. The 700 V DC bus voltage stems from a reference design within the SH2IPDRIVE project (SH2IPDRIVE 2024) and falls within the low voltage DC range (Latorre et al. 2023). The current control time constant of 1 ms matches typical control bandwidths of 1000 Hz as mentioned in Zeng et al. (2022). The voltage control bandwidth is chosen ten times slower to avoid interferences between the cascaded control loops. The output capacitances were estimated following the approach outlined in Tsakyridis et al. (2020).

4.1. Centralised control with LPF

As outlined in Section 3.2, a centralised PI controller with low-pass filter is implemented as a benchmark. The PI gains are tuned via pole

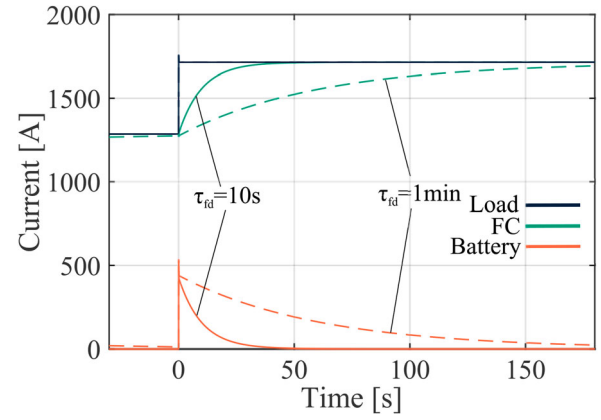


Figure 11. Total output current of FC and battery systems after a load step using the centralised PI control with LPF and time constants of 10 s (dashed) and 1 min (solid).

placement to match the desired voltage control bandwidth:

$$k_p = C_{dc} \tau_{vc} \quad (22)$$

$$k_i = \frac{k_p^2}{4C_{dc}} \quad (23)$$

Equations (22) and (23) show that the feedback gains are dependent on the estimate of the total DC bus capacitance. The estimation may differ from the real value. An overestimation will lead to a more aggressive control action, and vice versa. This fact should be accounted for in the control design to ensure sufficient stability margins. The low-pass filter is parameterised with the frequency decoupling time constant as $\tau_{LPF} = \tau_{fd}$. The reference currents are distributed among parallel components of the same type proportional to their power rating. Initially, all FCs and batteries are rated equally and accordingly the current is shared equally among parallel components. The figures with results show the summed currents of all components of the same type.

In the first simulation, the step response of the power system was investigated. Measurements of the propulsive power, taken during a mission of the reference cargo vessel, show an average load of 900 kW during cruising. Taking this value as the starting point, the step to full propulsive power of 1200 kW was investigated, matching load current increase from 1286 A to 1714 A at 700 V. Two cases with $\tau_{fd} = 10$ s and 1 min were analyzed to compare the effects of different time constants. The resulting trajectories are displayed in Figure 11. The FCs react to the load change according to the LPF; therefore at $t = \tau_{fd}$ the output current reaches 63.2% of the step. The battery supplies the remaining difference between load and FC power, and additionally stabilises the DC link voltage, which remains within 20 V of the nominal DC link voltage of 700 V.

4.2. Decentralised control strategy

The proposed strategy aims to achieve the same performance as the central controller using a decentralised architecture. For this purpose, the total droop resistance was chosen to equal the inverse of the proportional factor of the PI controller in the benchmark strategy. Furthermore, the time constant for frequency decoupling τ_{fd} is adjusted by sizing the virtual inductances and capacitances such that $\tau_{fd} = R_{d,rc} C_{d,rc} = L_{d,rl} / R_{d,rl}$.

In the first step, voltage regulation and SoC management are not implemented and the power system with the virtual impedance-based droop is subjected to the same load step as the benchmark strategy in Section 4.1. The simulation results in Figure 12 show that

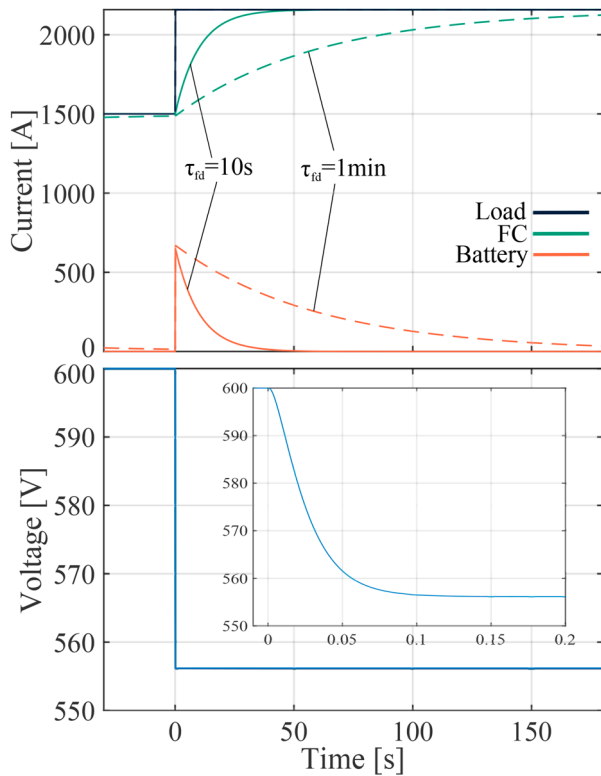


Figure 12. Load step response with decentralised strategy with $\tau_{fd} = 10$ s (dashed) and 1 min (solid) (a) FC, battery and load currents, (b) DC bus voltage.

frequency decoupling is achieved as accurately as with the benchmark, matching the chosen τ_{fd} . Since the load before the step is non-zero, the bus voltage has already decreased to 600 V due to the absence of an integral action. The steady-state deviation further increases to 144 V at full load. The reduced DC bus voltage requires higher currents and, therefore, increases conduction losses. In this case, the voltage drop is beyond 10 %, which would be a typical lower voltage limit. Furthermore, the power quality can be insufficient for sensitive loads, and a sudden change in voltage is challenging for accurate current control in DC-DC converters.

In the next step, the same step response as before was simulated with the proposed strategy, including the voltage regulation described in Section 3.3.2. The gain k_v in (11) was selected to match the integral action of the benchmark's PI controller:

$$k_v = \frac{\tau_{vc}}{4} \quad (24)$$

Note that the squared term present in the denominator in Equation (23) is not present here, since the adjusted voltage $V_{d,ref}$ is still passing through the droop controller. The step response obtained using this strategy is displayed in Figure 13. The resulting curves of the FC and battery currents are equal to those of the benchmark, indicating that the same behaviour of a centralised PI controller with an LPF can be achieved in a decentralised architecture. Additionally, this method achieves accurate tracking of the nominal DC bus voltage. Initially, after the load step, an acceptable voltage drop of 20.1 V can be observed, and the steady-state deviation could be eliminated.

Furthermore, Figure 13 shows the implications of changing the time constant τ_{fd} . With 1 min, a total of 2.44 kWh of battery charge is required to compensate for the difference between load and FC power, while the maximum current gradient of the FC systems is limited to 6.6 A/s. Reducing the time constant by a factor to 10 s proportionally reduced the required battery charge to 0.42 kWh.

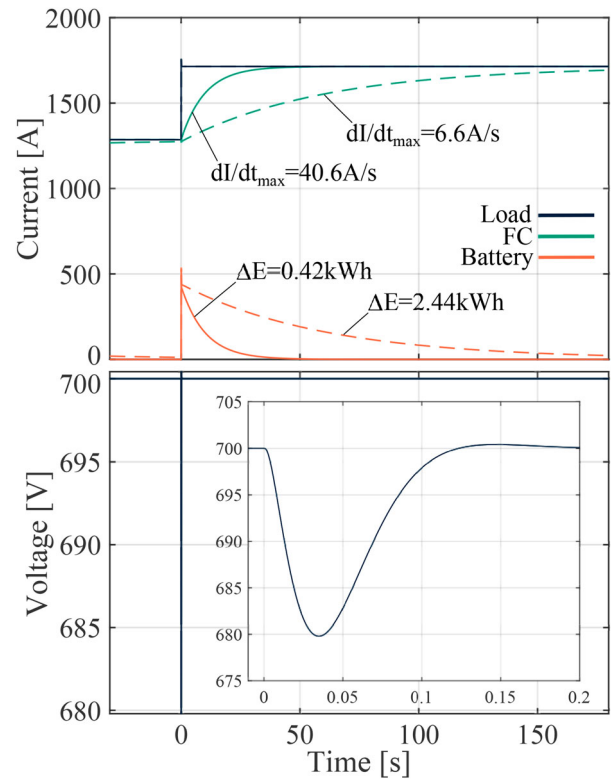


Figure 13. Load step response with decentralised strategy incl. voltage regulation with $\tau_{fd} = 30$ s (dashed) and 300 s (solid) (a) FC, battery and load currents, (b) DC bus voltage.

However, the current gradient of the FCs increased by the same factor to 40.6 A/s, leading to higher degradation. This comparison highlights the underlying trade-off between the required battery charge and dynamic operation of the FCs when selecting the time constant.

4.3. Mission simulation

The application of the proposed control strategy in an SPS is demonstrated using parts of real mission profiles as inputs. The challenging operation periods of the vessel occur during maneuvering, start-up and shutdown sequences, or other situations demanding highly fluctuating loads. Three scenarios are selected for which power profiles of the real operation are available. The first scenario represents a relatively short maneuvering sequence of ca. 2 h, which covers high power gradients. The second scenario covers the start-up and maneuvering out of harbour sequence until cruising. The third scenario, in turn, is the shutdown from cruising into the harbour. The latter two cover ca. 5 h of operation each. Figure 14 shows the power demand over time for all three scenarios.

Three mission simulations were performed for each scenario with different time constants τ_{fd} of 10 s, 1 min, and 10 min. Because multiple control functionalities act on the power system, it is key to ensure that they do not interfere with each other. An increased time constant aims at smoothing the FCs' output power while requiring the batteries to provide more power and depth-of-discharge for achieving the load-generation-balance. The current and voltage control bandwidths are separated by tuning the control parameters to meet the values listed in Table 3. In the same manner, the slower control loops, i.e. the frequency decoupling and the SoC management, need to be separated to avoid them interfering with one another. The shape factor α was set to 2.0 so that the slope of the charging current around

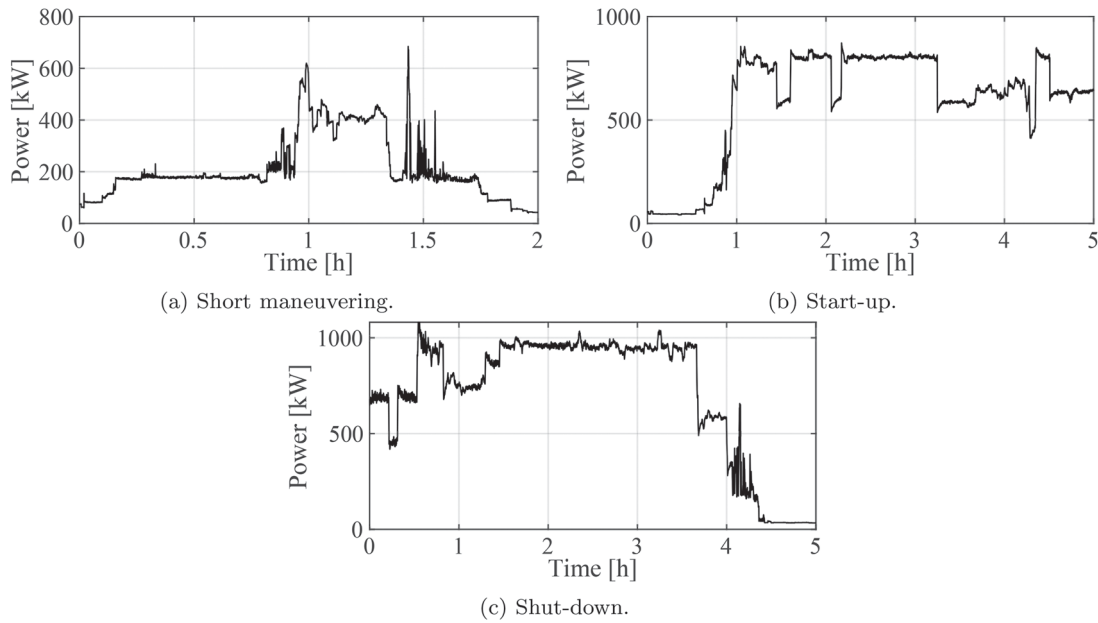


Figure 14. Exemplary power profiles obtained from measurements taken during the reference vessels' operation. (a) Short maneuvering. (b) Start-up and (c) Shut-down.

Table 4. Key values of simulation results with different frequency decoupling time constants for short maneuvering/start-up/shutdown profiles.

Value	Frequency decoupling time constant τ_{fd}		
	10 s	1 min	10 min
SoC_{min} [%]	49.7/49.7/49.5	48.4/47.6/47.8	42.1/32.3/33.0
SoC_{max} [%]	50.0/50.1/50.2	50.1/50.1/51.9	57.2/58.7/63.9
$P_{bat,min}$ [kW]	-255/-221/-325	-212/-256/-319	-274/-471/-435
$P_{bat,max}$ [kW]	232/159/252	387/287/262	320/468/409
$ P_{fc} _{avg}$ [W/s]	1083/1605/3148	731/1494/2929	693/1431/2841

the target SoC was flat. Doing so ensures that the SoC management acts more slowly than the frequency decoupling.

Resulting current trajectories of total FC and battery power, as well as battery SoC over time, are shown in Figures 15, 16, and 17, for the three scenarios respectively. The plots with the results are zoomed in on the time period where the highest load fluctuations occur. For the simulation, running at 1 ms steps, the measured values, sampled at 200 ms, were linearly interpolated.

Table 4 summarises the key numbers from the simulations, including the batteries' SoC ranges, as well as maximum charge and discharge currents. Load cycling is reported to be detrimental to the health of PEMFC (Pahon et al. 2019 oct; Jourdan et al. 2014 oct). In Fletcher et al. (2016), a linear degradation factor for transient loads on the cell voltage decay was used. Hence, the average absolute value of the FC power gradient $|P_{fc}|_{avg}$ is listed as a proxy for assessing the effect of transient FC operation on degradation. Given the FC output $P_{fc,n}$ and time at the n th simulation step t_n , it is computed as

$$|P_{fc}|_{avg} = \frac{1}{N} \sum_{n=1}^N \frac{|P_{fc,n} - P_{fc,n-1}|}{t_n - t_{n-1}} \quad (25)$$

The results show that the FC follows the load closely, and little power and energy are demanded from the batteries with a low time constant. However, a higher time constant smoothens the power output of the FCs, reducing their power gradients and, consequently, their degradation. With a higher time constant, the SoC-limits are exploited to a higher degree, leading to a reduced transient operation of the FCs. During maneuvering (Figure 15), the average FC power

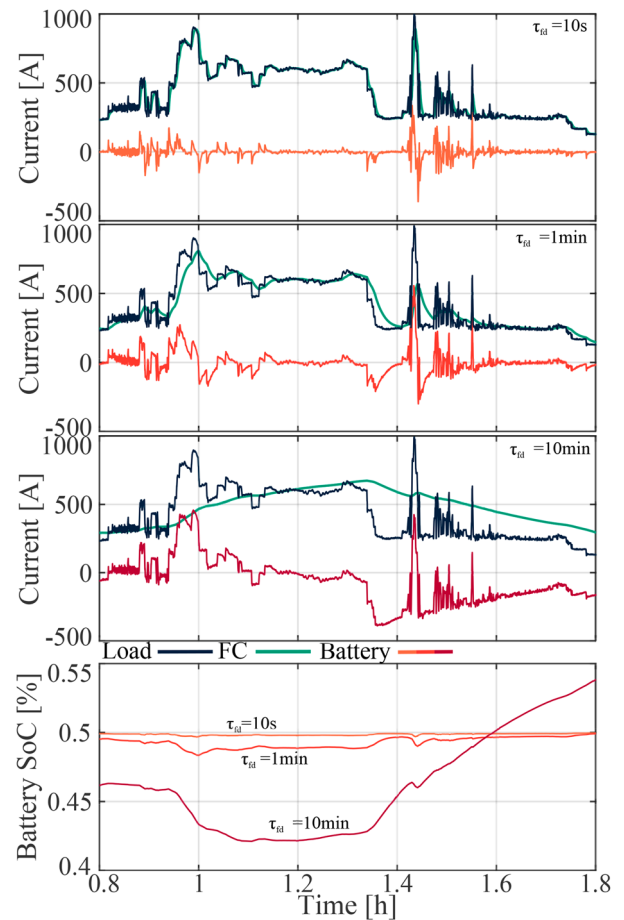


Figure 15. Power split between FCs and batteries and battery SoC during short maneuvering for different frequency decoupling time constants.

gradient is reduced by 32.5 % by increasing the time constant from 10 s to 1 min and even 36.0 % at 10 min. In the start-up (Figure 16) and shut-down (Figure 17) profiles, a minimum is reached when the

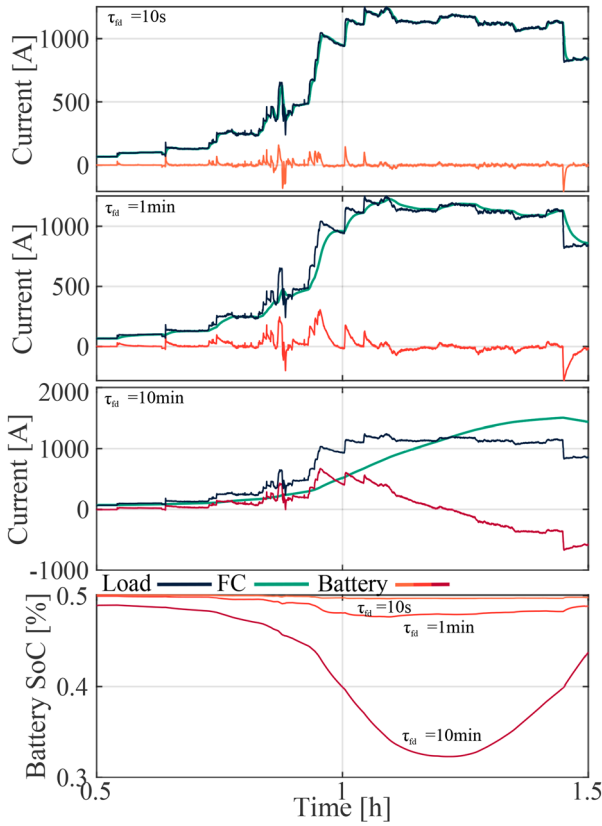


Figure 16. Power split between FCs and batteries and battery SoC start-up for different frequency decoupling time constants.

FC power is monotonously increasing or decreasing, respectively. It is to be noted that this metric does not consider the rate-of-change of the FC but the absolute change in output power.

The increased ESS discharge depth at higher time constants negatively influences the battery lifetime. The results underscore the importance of selecting the time constant to trade off the discharge depth of the batteries and the transient loading of the FCs. The simulated operation range of the batteries also shows that they may be sized significantly smaller when a small time constant is chosen to reduce capital expenditure.

4.4. Droop parameter adaptation

One key goal of the decentralised architecture is its adaptability to configuration changes and in this work the low bandwidth communication is leveraged to realise said adaptation. Accordingly, components with different ratings and characteristics should behave differently. To highlight this, the characteristics of the FC systems are changed to emulate aged components, which is done by shifting their polarisation curves down. Thereby their output voltage, and in turn their output power at a given current, is decreased. The voltage of FCs A, B, C and D are reduced by 0 %, 10 %, 20 % and 30 %, respectively. In addition, the batteries' capacities are changed to different ratings, and their initial SoCs are set to 40 % for battery A and 60 % for battery B. Accordingly, each component has an individual power rating, which influences the droop parameter calculation described in Section 3.4. Table 5 lists the parameters of the altered configuration. Non-listed parameters remain unchanged from the previous Section.

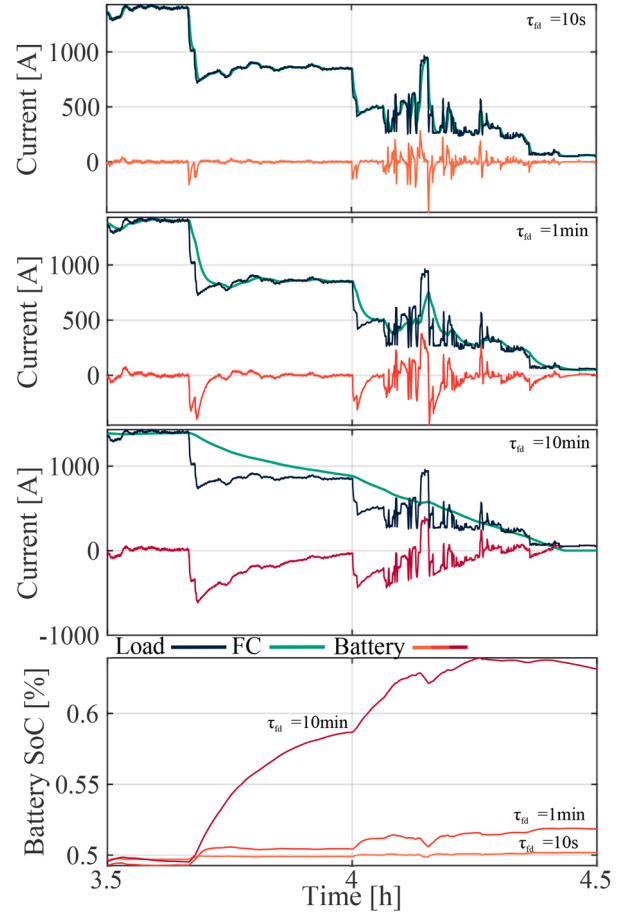


Figure 17. Power split between FCs and batteries and battery SoC during shutdown for different frequency decoupling time constants.

Table 5. Asymmetric component ratings and control parameterisation.

Parameter	Description	Value
$P_{r,fc,A}$	Power rating FC A	325.0 kW
$P_{r,fc,B}$	Power rating FC B	292.5 kW
$P_{r,fc,C}$	Power rating FC C	260.0 kW
$P_{r,fc,D}$	Power rating FC D	227.5 kW
$E_{bat,A}$	Energy capacity battery A	300 kWh
$P_{r,bat,A}$	Power rating battery A	450 kW
$E_{bat,B}$	Energy Capacity battery A	150 kWh
$P_{r,bat,B}$	Power rating battery B	225 kW
τ_{fd}	Frequency decoupling time constant	10 min

The power system is simulated with the short maneuvering power profile in Figure 14(a) to demonstrate the effectiveness of the proposed control architecture. The resulting output currents of all components and battery SoC are shown in Figure 18. Generally, the configuration changes lead, as expected, to an unequal current sharing among both the FCs as well as among the batteries. For both type of components, the current sharing is proportional to their power rating such that the FCs with higher maximum power carry higher currents. Analogously, battery A provides twice the current as battery B for voltage stabilisation, due to its doubled capacity and power rating. Additionally, it can be observed, that the SoC management strategy of both batteries lets both charges converge over time.

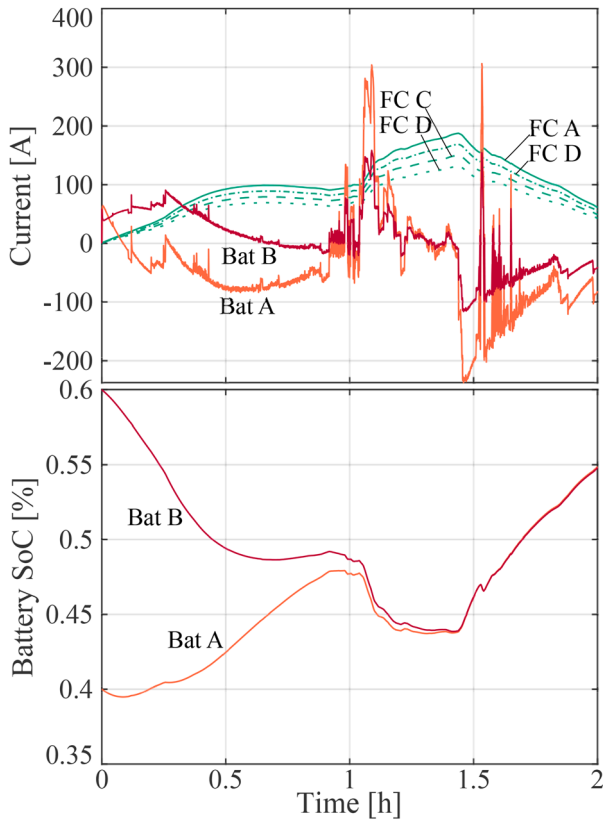


Figure 18. Power sharing and battery charge during mission simulation of short maneuvering with asymmetric component ratings and different initial SoC.

4.5. Reconfiguration after fault

The reconfiguration of the power system control is investigated by emulating component faults. As described in Section 3.4, the fault itself has three immediate effects on the coordinated control. First, the power output of the disconnected component drops to zero, creating a power imbalance which needs to be compensated. Second, the total DC bus capacity is reduced by the output capacity of the disconnected converter. Third, the total virtual resistance of the control strategy is increased since one local controller is missing. Thus, the time-response of the voltage stabilisation is slowed down.

Here, two successive faults of a battery system and a FC system are emulated. The disconnection of an ESS leads to an increased total virtual resistance of the high frequency power supplies, while the low-frequency resistance is affected by the FC fault. Three adaptation strategies are compared. First, no adaptation of parameters is done. Second, the parameters are adapted to track a reference value $R_{d,ref}$ with the total virtual resistance. Third, $R_{d,ref}$ is adapted according to Equation (21) to keep the voltage control at the desired bandwidth.

The two faults are sufficiently far apart, such that the first parameter adaptation is completed at the time of the second fault. Figure 19 shows the battery disconnection at $t = 0$ s. Since the fault instance the battery output is close to zero, the remaining battery is only required to compensate for a minor imbalance, yielding a voltage drop of ca. 3 V. Figure 19 shows the low- and high frequency elements of the total virtual resistance over time. The battery disconnection instantly doubles the high frequency element. This value remains unchanged if no adaptation is undergone, yielding differing virtual resistances of the low- and high frequency controllers. In the second case, the resistance converges back to its target value by

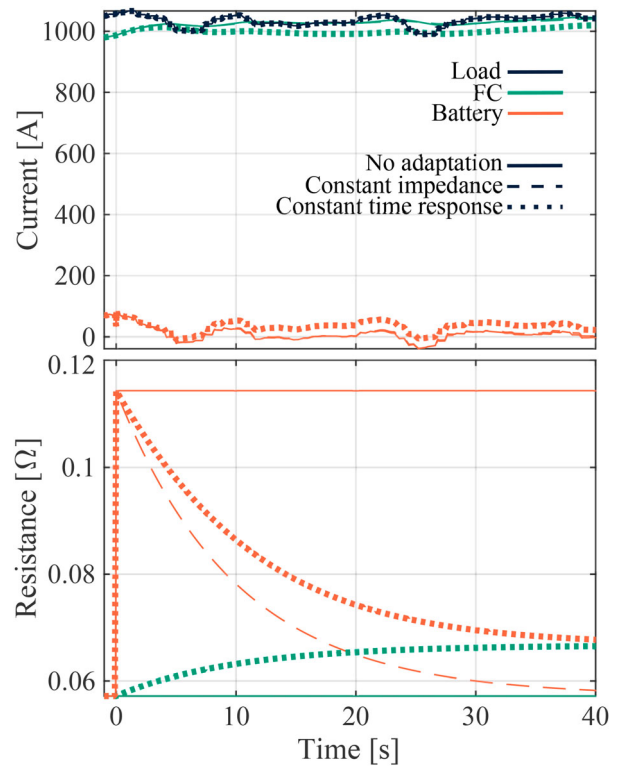


Figure 19. Droop resistances and current sharing immediately after battery fault for different adaptation scenarios.

decreasing the droop parameter of the remaining battery controller. In the third case, due to the decreased DC bus capacity, the total droop resistance is led to a slightly higher value than originally. Here, the low frequency components also adapt their droop parameters, reacting to the adapted DC bus capacity estimation. In the second and third cases, the final virtual resistance of all low- and high-frequency components matches, as intended in the implementation guidelines in Section 3.3.4.

During the subsequent FC system fault, the local controllers are parameterised differently, depending on the adaptation strategy. The results are shown in Figure 20, with the fault occurring at $t = 0$ s. A quarter of the delivered power is suddenly cut back and is required to be compensated by the remaining battery.

Figure 20 shows the voltage trajectories during the stabilisation for the three described strategies. With no adaptation, the total droop resistance is too high, leading to an increased voltage dip of 24 V and a subsequent overshoot after stabilisation. With a constant droop resistance in the second case, the voltage stabilisation becomes more aggressive, since the total droop resistance is lower than required to achieve the desired voltage control bandwidth, yielding a voltage dip of 13 V. Finally, in the third case, the voltage stabilisation is achieved as designed according to the voltage control bandwidth ω_{vc} , yielding a voltage dip of 15 V, 37.5 % lower than without parameter adaptation.

Figure 20 shows the droop parameter adaptation for the high bandwidth droop resistance after the fault. With the adaptation enabled, low- and high-frequency resistances converge towards the same value. The low bandwidth resistance remains constant except for the third case, where the system reacts to the change in DC bus capacity. Accordingly, for consistent behaviour, regardless of the system topology, an adaptation of the droop parameters following the desired voltage control bandwidth is recommended.

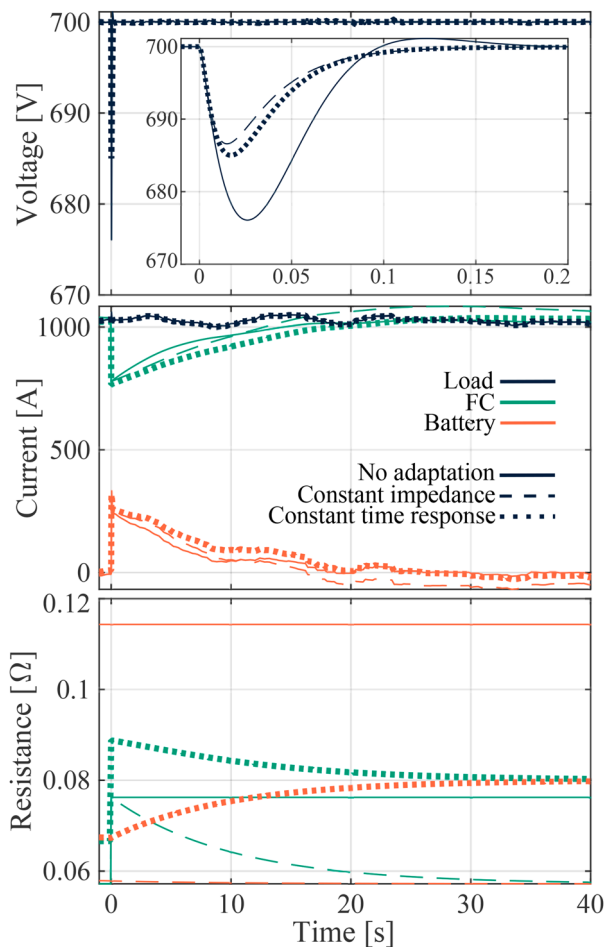


Figure 20. Voltage stabilisation, droop resistances and current sharing immediately after fuel cell fault with previous battery fault for different adaptation scenarios.

5. Conclusions

Although FC-battery hybrid power systems with DC distribution are emerging as a promising solution for zero-emission shipping, the coordinated control of multiple power system resources remains a challenge. In larger systems, a modular approach for integration and control is a viable approach, as it can facilitate the reconfiguration and extension of the SPS.

This work presented a decentralised coordinated control strategy using virtual impedance-based droop achieving low DC bus voltage deviations and fast restoration as well as a load frequency decoupling. It could be shown that the decentralised solution can achieve the same quality in dynamic power sharing and voltage control as a centralised PI controller with an LPF. The controller tuning affects the power gradients and load changes demanded from the FC systems, as well as the required depth-of-discharge for the ESS. Accordingly, a trade-off must be made between FC and ESS degradation arising from their dynamic operation. This study further presented an approach for automatic parameter adaptation after system reconfiguration utilising a low-bandwidth communication network. The adaptation is proposed as a means to facilitate a modular power system control. It could be shown the the power sharing among components is adapting to configuration and parameters alterations and furthermore the voltage dynamics of the electric system could be maintained after disconnection of multiple components.

Whereas a low-bandwidth communication network facilitates parameter adaptation, its full potential has not yet been leveraged.

The consideration of varying component parameters, e.g. owing to aging effects, and the consideration of different component types remain unaddressed topics for future research. This study considers simple component models for FCs and batteries, which allows parameterisation with limited manufacturer data. Such models are sufficient for this work's focus on the system dynamics of the electric distribution system. However, models with higher fidelity will enable to generate deeper insights in the component-level behaviour. Accurate quantification of FC and battery degradation, as well as hydrogen consumption of the proposed methodology, and a comparison to an optimised control strategy will be valuable additions in the future.

Acknowledgments

This article is an extension of the work presented in Kopka et al. (2023) at the *Modelling and Optimisation of Ship Energy Systems (MOSES) Conference 2023* in Delft, The Netherlands.

Disclosure statement

No potential conflict of interest was reported by the author(s).

Funding

This research is supported by the *Sustainable Hydrogen Integrated Propulsion Drives (SH2IPDRIVE)* project, which has received funding from Rijksoverheid (RvO) (reference number MOB21013), through the RDM regulation of the Ministry of Economic Affairs and Climate Policy.

ORCID

Timon Kopka  <http://orcid.org/0000-0002-0043-8446>

References

- Ahmadi Sarbast V. 2021. Modeling of proton exchange membrane fuel cell performance degradation and operation life [Thesis].
- Balestra L. 2022. Design of hybrid fuel cell/battery systems for maritime vessels [Doctoral Thesis]. NTNU.
- Balestra L, Schjøberg I. 2021. Energy management strategies for a zero-emission hybrid domestic ferry. *Int J Hydrogen Energy*. 46(77):38490–38503. doi: [10.1016/j.ijhydene.2021.09.091](https://doi.org/10.1016/j.ijhydene.2021.09.091)
- Bassam AM, Phillips AB, Turnock SR, Wilson PA. 2017. Development of a multi-scheme energy management strategy for a hybrid fuel cell driven passenger ship. *Int J Hydrogen Energy*. 42(1):623–635.
- Chen H, Zhang Z, Guan C, Gao H. 2020. Optimization of sizing and frequency control in battery/supercapacitor hybrid energy storage system for fuel cell ship. *Energy*. 197:117285.
- Chen X, Zhou J, Shi M, Yan L, Zuo W, Wen J. 2019. A novel virtual resistor and capacitor droop control for HESS in medium-voltage DC system. *IEEE Trans Power Syst*. 34(4):2518–2527.
- Dragicevic T, Lu X, Vasquez J, Guerrero J. 2015. DC microgrids—part i: a review of control strategies and stabilization techniques. *IEEE Transactions on Power Electronics*. 31(7):4876–4891.
- Fletcher T, Thring R, Watkinson M. 2016. An energy management strategy to concurrently optimise fuel consumption & PEM fuel cell lifetime in a hybrid vehicle. *Int J Hydrogen Energy*. 41(46):21503–21515. doi: [10.1016/j.ijhydene.2016.08.157](https://doi.org/10.1016/j.ijhydene.2016.08.157)
- Gao F, Kang R, Cao J, Yang T. 2019. Primary and secondary control in DC microgrids: a review. *Journal of Modern Power Systems and Clean Energy*. 7(2):227–242. doi: [10.1007/s40565-018-0466-5](https://doi.org/10.1007/s40565-018-0466-5)
- Geertsma R, Negenborn R, Visser K, Hopman J. 2017. Design and control of hybrid power and propulsion systems for smart ships: a review of developments. *Appl Energy*. 194:30–54. doi: [10.1016/j.apenergy.2017.02.060](https://doi.org/10.1016/j.apenergy.2017.02.060)
- Han J, Charpentier JF, Tang T. 2014. An energy management system of a fuel cell/battery hybrid boat. *Energies*. 7(5):2799–2820. doi: [10.3390/en7052799](https://doi.org/10.3390/en7052799)
- Han Y, Ning X, Yang P, Xu L. 2019. Review of power sharing, voltage restoration and stabilization techniques in hierarchical controlled DC microgrids. *IEEE Access*. 7:149202–149223. doi: [10.1109/Access.6287639](https://doi.org/10.1109/Access.6287639)
- Hansen JF, Wendt F. 2015. History and state of the art in commercial electric ship propulsion, integrated power systems, and future trends. *Proc IEEE*. 103(12):2229–2242. doi: [10.1109/JPROC.2015.2458990](https://doi.org/10.1109/JPROC.2015.2458990)
- Haseltalab A, van Biert L, Sapra H, Mestemaker B, Negenborn RR. 2021. Component sizing and energy management for SOFC-based ship power systems. *Energy Convers Manag*. 245:114625. doi: [10.1016/j.enconman.2021.114625](https://doi.org/10.1016/j.enconman.2021.114625)

- Jin Z, Meng L, Vasquez JC, Guerrero JM. 2017 Mar. Frequency-division power sharing and hierarchical control design for DC shipboard microgrids with hybrid energy storage systems. In: 2017 IEEE Applied Power Electronics Conference and Exposition (APEC), Tampa, FL, USA; p. 3661–3668.
- Jourdan M, Mounir H, El Marjani A. 2014 Oct. Compilation of factors affecting durability of Proton Exchange Membrane Fuel Cell (PEMFC). In: 2014 International Renewable and Sustainable Energy Conference (IRSEC), Ouarzazate, Morocco; p. 542–547.
- Khazaei J. 2021. Optimal flow of MVDC shipboard microgrids with hybrid storage enhanced with capacitive and resistive droop controllers. *IEEE Trans Power Syst.* 36(4):3728–3739. doi: 10.1109/TPWRS.2021.3049343
- Kopka T, Mylonopoulos F, Coraddu A, Polinder H. 2023. Decentralized power sharing with frequency decoupling for a fuel cell-battery dc shipboard power system. In: *Modelling and Optimisation of Ship Energy Systems 2023*.
- Kwon K, Park D, Zadeh MK. 2020 Jun. Load frequency-based power management for shipboard dc hybrid power systems. In: 2020 IEEE 29th International Symposium on Industrial Electronics (ISIE), Delft, Netherlands; p. 142–147.
- Latorre A, Soeiro TB, Geertsma R, Coraddu A, Polinder H. 2023. Shipboard DC systems –critical overview: challenges in primary distribution, power-Electronics-Based protection, and power scalability. *IEEE Open J Ind Electron Soc.* 4:259–286. doi: 10.1109/OJIES.2023.3294999
- Lu X, Guerrero JM, Sun K, Vasquez JC. 2014. An improved droop control method for DC microgrids based on low bandwidth communication with DC bus voltage restoration and enhanced current sharing accuracy. *IEEE Trans Power Electron.* 29(4):1800–1812. doi: 10.1109/TPEL.2013.2266419
- Mokhtar M, Marei MI, El-Sattar AA. 2019. An adaptive droop control scheme for DC microgrids integrating sliding mode voltage and current controlled boost converters. *IEEE Trans Smart Grid.* 10(2):1685–1693. doi: 10.1109/TSG.5165411
- Mutarrif MU, Terriche Y, Niazi KAK, Vasquez JC, Guerrero JM. 2018. Energy Storage Systems for Shipboard Microgrids—A Review. *Energies.* 11(12):3492.
- Mylonopoulos F, Kopka T, Coraddu A, Polinder H. 2024. A model-based parametric study for comparison of system configurations and control of a hydrogen hybrid cargo vessel. In: *Modelling and Optimisation of Ship Energy Systems 2023*, Delft, Netherlands.
- Nedstack. 2023 Jul. Nedstack | FCS 13-XXL; [<https://nedstack.com/en/pem-fcs-stack-technology/fcs-13-xxl>].
- Njoya S, Tremblay O, Dessaint LA. 2009 Sep. A generic fuel cell model for the simulation of fuel cell vehicles. In: 2009 IEEE Vehicle Power and Propulsion Conference, Dearborn, MI, USA; p. 1722–1729.
- Nuchturee C, Li T, Xia H. 2020. Energy efficiency of integrated electric propulsion for ships – A review. *Renew Sustain Energy Rev.* 134:110145. doi: 10.1016/j.rser.2020.110145
- Pahon E, Jemei S, Steiner NY, Hissel D. 2019 Oct. Effect of load cycling on the performance of fuel cell stacks. In: 2019 IEEE Vehicle Power and Propulsion Conference (VPPC), Hanoi, Vietnam; p. 1–4.
- Peyghami S, Mokhtari H, Davari P, Loh PC, Blaabjerg F. 2017. On secondary control approaches for voltage regulation in DC microgrids. *IEEE Trans Ind Appl.* 53(5):4855–4862. doi: 10.1109/TIA.2017.2704908
- Sadabadi MS, Shafiee Q, Karimi A. 2018. Plug-and-Play robust voltage control of DC microgrids. *IEEE Trans Smart Grid.* 9(6):6886–6896. doi: 10.1109/TSG.2017.2728319
- SH2IPDRIVE. 2024. Sustainable hydrogen integrated propulsion drives; [<http://sh2ipdrive.com/>].
- Shakeri N, Zadeh M, Bremnes Nielsen J. 2020. Hydrogen fuel cells for ship electric propulsion: moving toward Greener ships. *IEEE Electr Mag.* 8(2):27–43. doi: 10.1109/MELEC.6508996
- Su CL, Weng XT, Ching-Jin C. 2014 Aug. Power generation controls of fuel cell/energy storage hybrid ship power systems. In: 2014 IEEE Conference and Expo Transportation Electrification Asia-Pacific (ITEC Asia-Pacific); Beijing, China: IEEE. p. 1–6.
- Tremblay O, Dessaint LA, Dekkiche AI. 2007 Sep. A generic battery model for the dynamic simulation of hybrid electric vehicles. In: 2007 IEEE Vehicle Power and Propulsion Conference, Arlington, TX, USA; p. 284–289.
- Tsakyridis G, Xiros NI, Scharringhausen M, Witte L. 2020. Design and control of a DC boost converter for fuel-cell-powered marine vehicles. *J Mar Sci Appl.* 19(2):246–265. doi: 10.1007/s11804-020-00140-8
- van Biert L, Godjevac M, Visser K, Aravind P. 2016. A review of fuel cell systems for maritime applications. *J Power Sources.* 327:345–364. doi: 10.1016/j.jpowsour.2016.07.007
- Xiao ZX, Guan YZ, Fang HW, Terriche Y, Guerrero JM. 2022. Dynamic and steady-state power-sharing control of high-efficiency DC shipboard microgrid supplied by diesel generators. *IEEE Syst J.* 16(3):4595–4606. doi: 10.1109/JSYST.2021.3111685
- Xie P, Tan S, Bazmohammadi N, Guerrero Josep M, Vasquez Juan C, Alcalá JM, Carreño JEM. 2022. A distributed real-time power management scheme for shipboard zonal multi-microgrid system. *Appl Energy.* 317:119072. doi: 10.1016/j.apenergy.2022.119072
- Xing H, Stuart C, Spence S, Chen H. 2021. Fuel cell power systems for maritime applications: progress and perspectives. *Sustainability.* 13(3):1213. doi: 10.3390/su13031213
- Xu L, Guerrero J, Lashab A, Wei B, Bazmohammadi N, Vasquez J, Abusorrah A. 2022. A review of DC shipboard microgrids –control architectures, stability analysis, and protection schemes. *IEEE Trans Power Electron.* 37(4):4105–4120. doi: 10.1109/TPEL.2021.3128409
- Xu L, Guerrero J, Lashab A, Wei B, Bazmohammadi N, Vasquez J, Abusorrah A. 2022. A review of DC shipboard microgrids –power architectures, energy storage, and power converters. *IEEE Trans Power Electron.* 37(5):5155–5172. doi: 10.1109/TPEL.2021.3128417
- Xu Q, Hu X, Wang P, Xiao J, Tu P, Wen C, Lee MY. 2017. A decentralized dynamic power sharing strategy for hybrid energy storage system in autonomous DC microgrid. *IEEE Trans Ind Electron.* 64(7):5930–5941. doi: 10.1109/TIE.2016.2608880
- Zahedi B, Norum LE. 2013a. Modeling and simulation of all-electric ships with low-voltage DC hybrid power systems. *IEEE Trans Power Electron.* 28(10):4525–4537. doi: 10.1109/TPEL.2012.2231884
- Zahedi B, Norum LE. 2013b Sep. Voltage regulation and power sharing control in ship LVDC power distribution systems. In: 2013 15th European Conference on Power Electronics and Applications (EPE), Lille, France; p. 1–8.
- Zahedi B, Norum LE, Ludvigsen KB. 2014. Optimized efficiency of all-electric ships by dc hybrid power systems. *J Power Sources.* 255:341–354. doi: 10.1016/j.jpowsour.2014.01.031
- Zeng H, Zhao Y, Wang X, He T, Zhang J. 2022. Modeling of ship DC power grid and research on secondary control strategy. *J Mar Sci Eng.* 10(12):2037. doi: 10.3390/jmse10122037
- Zhu L, Han J, Peng D, Wang T, Tang T, Charpentier JF. 2014 Mar. Fuzzy logic based energy management strategy for a fuel cell/battery/ultra-capacitor hybrid ship. In: 2014 First International Conference on Green Energy ICGE, Sfax, Tunisia 2014; p. 107–112.